Dalton Transactions

ROYAL SOCIETY OF CHEMISTRY

PAPER

View Article Online
View Journal | View Issue

Check for updates

Cite this: *Dalton Trans.*, 2023, **52**, 15871

Effects of oxygen functionalities on hydrous hydrazine decomposition over carbonaceous materials†

Silvio Bellomi, [a] Ilaria Barlocco,[a] Simone Tumiati,[b] Patrizia Fumagalli,[b] Nikolaos Dimitratos, [c,d] Alberto Roldan *[e] and Alberto Villa *[a]

Received 20th July 2023,
Accepted 17th September 2023

DOI: 10.1039/d3dt02310a

rsc.li/dalton

Metal-free heterogeneous catalysis is promising in the context of H_2 generation. Therefore, establishing structure–activity relationships is a crucial issue to improve the development of more efficient catalysts. Herein, to evaluate the reactivity of the oxygen functionalities in carbonaceous materials, commercial functionalized pyrolytically stripped carbon nanofibers (CNFs) were used as catalysts in the liquid-phase hydrous hydrazine decomposition process and its activity was compared to that of a pristine CNF material. Different oxygenated groups were inserted by treating CNFs with hydrogen peroxide for 1 h (O1-H_2O_2) and HNO_3 for 1 h (O1-HNO_3) and 6 h (O6-HNO_3). An increase in activity was observed as a function of the oxidizing agent strength (HNO_3 > H_2O_2) and the functionalization time (6 h > 1 h). A thorough characterization of the catalysts demonstrated that the activity could be directly correlated with the oxygen content (O6-HNO_3 > O1-HNO_3 > O1-H_2O_2 > CNFs) and pointed out the active sites for the reaction at carbon–oxygen double bond groups (C═O and COOH). Systematic DFT calculations supported rationalization of the experimental kinetic trends with respect to each oxygen group (C═O, C–O–C, C–OH and COOH).

Introduction

The search for sustainable chemical processes is crucial for achieving a resilient society. Alongside this, the global energetic demand is steadily increasing, raising the necessity for higher energy generation capacities, better management and efficiency of generated energy, and lower dependence on non-renewable fossil fuels.[1]

Molecular hydrogen is recognized as one of the most promising clean energy sources due to its high intrinsic energy density and innocuous by-products upon utilization. Hydrogen can be produced through several methods, including photocatalytic and electro-catalytic systems, steam reforming and biomass-, coal- or natural gas-based processes.[1] Even though the benefits of hydrogen are apparent, its direct usage is limited by the lack of economically sustainable and safe storage and transportation technologies.[2] Typically, storage procedures require pressurized tanks, both for gaseous or liquified hydrogen, whose applicability is restricted by low efficiencies and high costs.[3,4]

Liquid Hydrogen Carriers (LHCs) are easily storable and transportable chemical compounds with a high intrinsic hydrogen content, which can be released chemically, desirably under mild conditions. Many LHCs exist, but the need to reduce CO_2 emissions has led to a focus on nitrogen–hydrogen compounds. N_2H_4 possesses a hydrogen content of 12.5 wt%.[5] Nonetheless, given its intrinsic hypergolic nature, *i.e.*, serious risk of explosions in the presence of certain metals,[6] it is handled in the hydrated form, hydrous hydrazine ($N_2H_4 \cdot H_2O$, 8 wt% hydrogen content).[7,8] $N_2H_4 \cdot H_2O$ is reported to decompose catalytically through two different pathways:[9]

$$N_2H_4 \rightarrow N_2(g) + 2H_2(g) \quad \Delta H° = -95.4 \text{ kJ mol}^{-1} \tag{1}$$

$$3N_2H_4 \rightarrow N_2(g) + 4NH_3(g) \quad \Delta H° = -157.0 \text{ kJ mol}^{-1} \tag{2}$$

The first reaction (eqn (1)) represents the complete reforming pathway, where molecular hydrogen and nitrogen are produced. The second path (eqn (2)) produces nitrogen and ammonia and is the thermodynamically favoured process.

---

[a] *Dipartimento di Chimica, Università degli Studi di Milano, via Golgi 19, I-20133 Milano, Italy. E-mail: alberto.villa@unimi.it*
[b] *Dipartimento di Scienze della Terra Ardito Desio, Università degli Studi di Milano, via Mangiagalli 34, Milano I-20133, Italy*
[c] *Dipartimento di Chimica Industriale "Toso Montanari", Alma Mater Studiorum Università di Bologna, Viale Risorgimento 4, Bologna 40126, Italy*
[d] *Center for Chemical Catalysis-C3, Alma Mater Studiorum Università di Bologna, Viale Risorgimento 4, Bologna 40136, Italy*
[e] *Cardiff Catalysis Institute, School of Chemistry, Cardiff University, Main Building, Park Place, CF10 3AT Cardiff, UK. E-mail: RoldanMartinezA@cardiff.ac.uk*

† Electronic supplementary information (ESI) available. See DOI: **https://doi.org/10.1039/d3dt02310a**

Several studies focused on using noble[10,11] and non-noble[12,13] metal-based catalysts to promote hydrazine decomposition. These investigations highlighted a dependence of the reaction selectivity upon the catalyst's nature and the reaction parameters, *e.g.*, pressure, temperature, and stirring.[11,14–17] Despite the catalytic activity presented, the carbon fingerprint and scalability of the metal catalysts are questionable due to their mining and manufacturing methods and scarcity. Therefore, it is advised to design new metal-free catalysts for a sustainable future.[18]

Carbon-based materials are attracting significant attention as catalysts due to their high tunability. Facile changes in their lattice structure allow significant variations of, for instance, surface area, porosity, functional groups and topological defects.[19] Of particular interest are those metal-free carbo-catalysts that successfully generated hydrogen in the liquid phase from different substrates, including alkenes, alkanes and formic acid.[20,21]

Several works focused on the hydrazine-mediated reduction of different target substrates.[22–24] Remarkable results were obtained for the reduction of nitroarenes performed over carbo-catalysts.[25] Fujita and co-workers[26] complemented these results unveiling the effect of N and O functionalities. The introduction of dopants induced changes in the surface properties of the carbons, enhancing the catalytic properties of the carbo-catalysts, *i.e.*, conversions and selectivity of the target substrates.

Previous investigations on the activity of carbonaceous materials' intrinsic defects for hydrous hydrazine decomposition unveiled fully that pyrolytically stripped carbon nanofibers (CNFs) exhibited the best performances among the tested carbo-catalysts thanks to a high degree of intrinsic defects, resulting in complete conversion of hydrous hydrazine up to 6 h of reaction with 89% H_2 selectivity.[27] Despite previous works and to the best of our knowledge, the literature lacks investigations rationalizing the effects of oxygen functionalities in metal-free carbonaceous materials for the decomposition of hydrous hydrazine.

The work presented here focuses on the liquid-phase oxygen functionalization of CNFs through different procedures and unveils their role in hydrous hydrazine decomposition. The nature of oxygen groups was modulated by employing different oxidizing agents (H_2O_2 and HNO_3) at variable functionalization times (1 and 6 h), resulting in O1-H_2O_2, O1-HNO_3, and O6-HNO_3. The functionalized carbo-catalysts were tested as catalysts under mild conditions, and their activity was compared with that of the pristine CNFs. To understand the effect of the functionalization procedures on the carbonaceous materials, fresh and spent catalysts were thoroughly characterized through ICP, Raman and XPS in combination with computational techniques.

Experimental

Materials and chemicals

Pyrolytically stripped carbon nanofibers (CNFs) were purchased from the Applied Science Company. Hydrous hydrazine ($N_2H_4 \cdot H_2O$, 98%), sodium hydroxide (NaOH, ≥98%), nitric acid (HNO_3, 65%) and hydrogen peroxide (H_2O_2, 30%) were acquired from Sigma-Aldrich.

Catalyst synthesis

In a typical functionalization procedure, 1 g CNFs were dispersed in 200 ml of the desired oxidizing agent (HNO_3 65% or H_2O_2 30%) in a 500 ml round bottom flask. Two different oxidizing agents were employed, namely HNO_3 and H_2O_2. For the HNO_3 treatment, a 353 K temperature and an 800 rpm stirring rate were employed, and the mixture was left for the desired time (1 or 6 h), resulting in O1- and O6-HNO_3, respectively. Differently, for the H_2O_2 treatment, the functionalization was performed at RT and with a stirring rate of 800 rpm for 1 h, leading to O1-H_2O_2. A longer functionalization time with H_2O_2 (6 h) did not produce significantly different kinetic results from the 1 h functionalized carbons; thus, we excluded O6-H_2O_2 from the proposed investigation.

Catalytic tests

Liquid phase $N_2H_4 \cdot H_2O$ decomposition was performed at a constant reaction temperature of 323 K using a 50 mL three-necked round bottom flask, with one of the flask's necks connected to a burette for the volumetric analysis of the gaseous products. Typically, the desired amount of catalyst (hydrous hydrazine/catalyst wt. ratio 16/1) was added in the reactor in the presence of 16.0 mL of a 0.5 M NaOH aqueous solution, and equilibrated at a stirring rate of 1400 rpm. Then, 600 μL of a 3.3 M aqueous solution of hydrous hydrazine was injected. Hydrous hydrazine conversion was analysed through a Jasco V-730 spectrophotometer, using a 1 cm quartz cell, based on the quantitative reaction of $N_2H_4 \cdot H_2O$ with 4-dimethylaminobenzaldehyde (4-DMAB) in dilute hydrochloric acid (HCl), resulting in a *p*-quinone structure that strongly absorbs radiation at 456 nm (Fig. 1).[28] The volume of gas produced was measured using the water displacement method. In a typical experiment, the reactor was connected with a tube fitted under a flipped burette, filled with water, and placed in a beaker containing H_2O. During the evolution, the gases were allowed to pass into a 0.05 M HCl aqueous solution to ensure the removal of NH_3, if any. Therefore, we quantified the evolved gaseous products (H_2 and N_2) from the volume of water displaced within the burette.[27]

Catalyst characterization

Functionalized carbon materials were characterized by Raman spectroscopy and X-ray Photoelectron Spectroscopy (XPS).

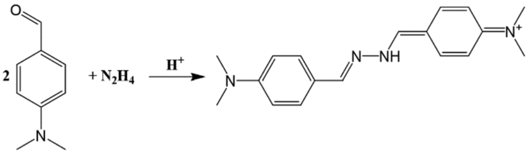

Fig. 1 Reaction of 4-DMAB and hydrous hydrazine to obtain the UV-Vis detectable *p*-quinone.

Raman spectroscopy was performed at the Department of Earth Sciences – University of Milan, using a Horiba LabRam HR Evolution micro-Raman spectrometer equipped with a green solid-state laser (532 nm) focused through a 100× objective, giving a spatial resolution of approximately 1 μm. The micro-Raman system was set with a 600 lines per mm grating and a hole of size 300 μm; the spectrum was collected with a final laser power of about 0.05 mW. The sample surface was measured through a hand-held power meter. Spectra were calibrated using the 520.7 cm^{-1} line of a silicon wafer. The sample was scanned at an exposure time of 300 s, and two accumulations were performed, giving a spectrum. XPS measurements were performed with a Thermo Scientific K-alpha+ spectrometer. The samples were analysed using a monochromatic Al X-ray source operating at 72 W, with the signal averaged over an oval-shaped area of 600 × 400 μm. Data were recorded at 150 eV for survey scans and 40 eV for high-resolution (HR) scans with a 1 eV and 0.1 eV step size, respectively. CASAXPS (v2.3.17 PR1.1) was used to analyse the XPS raw data. The C1s and O1s XPS core levels were fitted in agreement with models previously reported in the literature.[29] The presence of possible residual metal was analysed by inductively coupled plasma optical emission spectroscopy (ICP-OES) using a PerkinElmer Optima 8000 emission spectrometer.

Computational details

Plane-wave density functional theory (DFT) calculations were performed using the Vienna *Ab initio* Simulation Package (VASP).[30,31] A generalized gradient in the revised Perdew–Burke–Ernzerhof approximation functional (rPBE)[32] was employed to evaluate the correlation-exchange electronic contributions, with a kinetic energy cutoff of 500 eV chosen for the expansion of the Kohn–Sham valence state plane-waves.[33] rPBE is found to be efficient in modelling surface adsorption processes.[32] In addition, the VASP implementation of the rPBE functional improves the previous revPBE implementation,[34] fulfilling the Lieb–Oxford criterion globally by construction without any additional fitted parameter. All the calculations included the long-range dispersion correction approach by the Grimme DFT-D3 methods.[35,36] The implicit polarizable continuum solvation model, as implemented in VASPsol,[37,38] was included in all the calculations. The optimization thresholds were 10^{-5} eV and 0.02 eV $Å^{-1}$ for electronic and ionic force relaxation. For the Brillouin zone (BZ) sampling, a Γ-centred *k*-point mesh generated through the Monkhorst–Pack method of dimensions 5 × 5 × 1 was employed.[39] A first-order Methfessel–Paxton method was used with an energetic width value of 0.1 eV to ease the BZ sampling and improve the wavefunction convergence. All carbon-based materials were modelled starting from a single layer slab of a 6 × 6 pristine graphene supercell, where a single vacancy (SV) was introduced and functionalized with different O-containing groups, namely carbonylic (C═O), esteric (C–O–C), hydroxylic (C–OH) and carboxylic (COOH) moieties (Fig. S1†), in agreement with the XPS fitting model employed.[29] The supercell is in a hexagonal crystalline system with unit cell vectors *a* and *b* lying in the surface plane (γ = 120°) and perpendicular to the *c* axis. Both *a* and *b* were optimized at 2.46 Å, in good agreement with the experimental values obtained by HR-TEM for carbon materials.[40] A polarizable continuum dielectric bath of ~16 Å perpendicular to the C-surface was introduced to avoid spurious periodic interactions. The adsorption energy (E_{ads}) was defined as the difference between the combined system and the isolated species. Gibbs energies of adsorption (G_{ads}) were evaluated by adding zero-point energy corrections and entropy terms (details can be found in the ESI†).[41] The G_{ads} values were calculated in the harmonic approximation, while the entropy of hydrous hydrazine was obtained from the international tables.[42] The entropies of solid-state species were considered negligible.[43] All thermal corrections were made at the reaction temperature (323 K).

Results and discussion

Structure

The effect of oxygen functionalities on the hydrous hydrazine decomposition was investigated by modulating the nature of the oxidizing agent and the functionalization time on pristine carbon nanofibers (CNFs). As reported in the literature, a strong oxidizing agent such as nitric acid (HNO_3) can preferentially introduce carboxylic/carbonylic (C═O/COOH) species proportional to the functionalization time, whereas a milder oxidizing strength compound, *e.g.*, hydrogen peroxide (H_2O_2), increases the hydroxylic/esteric (C–OH/–C–O–C) group content.[44]

All the catalysts were thoroughly characterized through ICP-OES, Raman spectroscopy and XPS to disclose the catalysts' structure–activity relationship. The results from the ICP-OES analysis confirmed the absence of metal impurities in the catalysis of the hydrous hydrazine decomposition.[10,45] Raman spectroscopy evaluated the effect of the functionalization procedures on the catalyst morphology.[27] Commonly, carbon materials present two characteristic bands at around 1600 cm^{-1} (G band) and 1350 cm^{-1} (D band), and their intensity ratio (I_D/I_G) is commonly used as a descriptor of the defect density. In fact, the G band intensity correlates with structurally ordered graphite domains. The D band is symmetry forbidden and only allowed in structural defects or in-plane substitutional heteroatoms.[46] The comparable I_D/I_G ratios between the functionalized carbons and CNFs allowed us to infer that the functionalization procedures did not induce modification in the carbon framework, *i.e.*, substitutional heteroatoms, Fig. S2 and Table S1,† excluding the influence of additional intrinsic defects for the hydrous hydrazine decomposition. XPS provided information on the oxygen functionalities from analyses of the C1s and O1s core levels. The treatment with 6 h in HNO_3 introduced the highest quantity of oxygen groups (O/C = 0.157, O6-HNO_3), followed by the treatment for 1 h in HNO_3 (O/C = 0.141, O1-HNO_3) and 1 h in H_2O_2 (O/C = 0.141, O1-H_2O_2). All the procedures increased the number of oxygen functionalities with respect to the pristine material (O/C = 0.122, CNFs). The results are summarised in Table S1.†

We carried out a quantitative assessment of surface oxygen through high-resolution (HR) XPS analyses, focused on the O1s and C1s core levels to obtain more insights into the type of oxygen and surface content of each group.[47–49] Based on previously reported models, five peaks were considered for the O1s region as a function of their binding energies (BE).[29] The peaks at 531.1–531.8 eV can be assigned to carbon–oxygen double bonds (C═O), those at 532.4–532.7 eV to carbon–oxygen ether-like single bonds (C–O–C), and those at 533.3–533.6 eV to carbon–oxygen bonds in hydroxylic moieties (C–OH). Carboxylic moieties (COOH) are in the BE region of 532.0–533.0 eV, presenting an intermediate character between single and double bonds. A broad peak at about 535.2 eV is assigned to residual adsorbed water on the catalyst's surface. The results of the O1s core level fitting are summarised in Fig. 2. The C1s core levels, Fig. S4 and Table S3,† agree with the O1s data.

Functionalizing CNFs with H_2O_2 for 1 h (O1-H_2O_2) increased the ether-like (C–O–C) and hydroxylic (C–OH) groups to 23.1 and 18.2% compared to 19.5 and 14.3% in the initial CNFs, Fig. 2 and Table S2.† Differently, the HNO_3 functionalization of CNFs, at both 1 h (O1-HNO_3) and 6 h (O6-HNO_3), led to the preferential formation of carbonylic (C═O, 28.6 and 37.6% *vs.* 26.6% in the original CNFs) and carboxylic groups (COOH, 37.8 and 44.4% *vs.* 32.2% in CNFs). These results align with the higher oxidation strength of HNO_3 than that of H_2O_2, Table S2,† and with previous reports.[44,50]

Activity

The hydrous hydrazine decomposition on each catalyst was studied in a batch reactor under mild conditions (323 K and 1 atm). The conversions were quantified through the UV-Vis analysis of hydrous hydrazine quantitatively reacted with a colorimetric reagent (Fig. 1). At the same time, the selectivity towards H_2 production was calculated *via* the water displacement method when gas evolution reached a plateau, *i.e.*, the end of the decomposition reaction. The kinetic results are represented in Fig. 3, showing that at 150 minutes of reaction, O6-HNO3 resulted in the highest catalytic conversion (89%), followed by O1-HNO_3 (65%), O1-H_2O_2 (52%), and CNFs (45%). The O6-HNO_3 sample completed the conversion within 210 minutes of reaction, much faster than other catalysts (360 minutes). The enhanced activity in the presence of oxygen functionalities agrees with previous works on functionalized carbons for the hydrazine-mediated H transfer to nitroarenes.[25,26] Differently, we observed a decrease in H_2 production concerning the oxidizing agent strength and functionalization time (O6-HNO_3, 8% < O1-HNO_3, 14% < O1-H_2O_2, 35% < CNFs, 89%). Therefore, we postulate that the reported enhanced hydrogen transfer in the presence of oxygen functionalities[25,26] is due to the hydrous hydrazine decomposition intermediates, capable of transferring H more readily to the reduction targets.

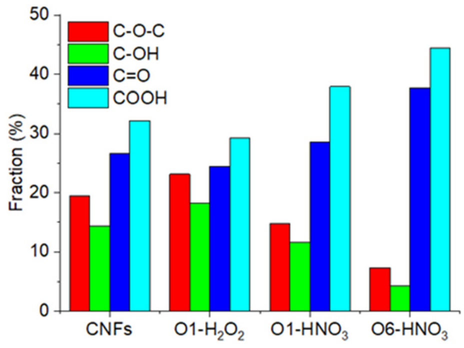

Fig. 2 HR-XPS analysis of the O1s region and speciation of the oxygen-containing functional groups for the different catalysts.

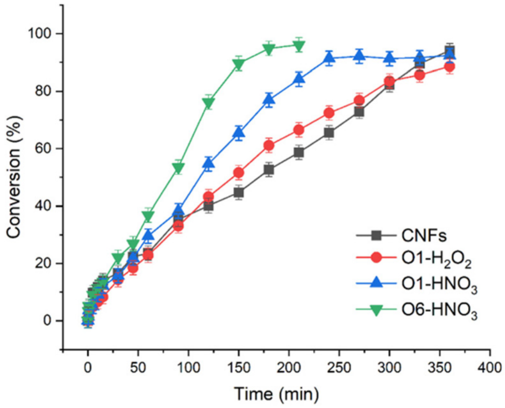

Fig. 3 Conversion trend in the hydrazine decomposition reaction for the different catalysts: CNFs (black), O1-HNO_3 (blue), O6-HNO_3 (green) and O1-H_2O_2 (red). All the tests were performed at 323 K and 1400 rpm, using 600 μL of a 3.3 M hydrazine solution in 16 mL of 0.5 M NaOH and a $N_2H_4 \cdot H_2O$: catalyst weight ratio of 16 : 1.

Structure–activity relationship

The oxygen content is linearly correlated with the catalytic activity (89%, O6-HNO_3 > 65%, O1-HNO_3 > 52%, O1-H_2O_2 > 52%, CNFs). Thus, confirming the active role of the oxygen groups in the hydrous hydrazine decomposition, Fig. 4a. However, the greater the number of oxygen functionalities, the lower the selectivity towards H_2 (8%, O6-HNO_3 < 14%, O1-HNO_3 < 35%, O1-H_2O_2 < 89%, CNFs), although no linear correlation has been observed, Fig. 4b. Table S1† summarises the structural features (O/C ratio

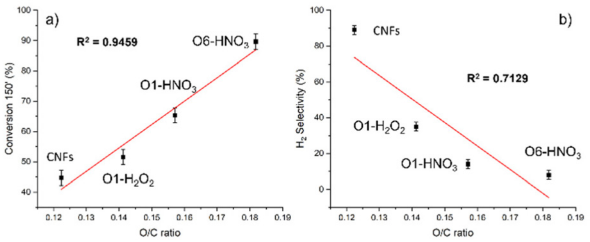

Fig. 4 The trends of (a) conversion at 150′ and (b) H_2 selectivity concerning the oxygen content (O/C ratio) derived from XPS analyses. Insets are the catalyst labels and R^2 factor of the linear fit.

from XPS and I_D/I_G from Raman) of the different catalysts considered and catalytic conversions at 150 minutes and H_2 selectivity at the end of the reaction. We plotted the N_2H_4 conversion as a function of the total surface content of each functional group in Fig. 5 to identify the active site for the reaction. A positive correlation was found between the conversion and the concentrations of C═O (R^2 = 0.9708) and COOH (R^2 = 0.9883). On the other hand, a content increase of C–O–C (R^2 = 0.8726) and C–OH (R^2 = 0.9117) decreases the catalytic performances. These results lead to the conclusion that carbon–oxygen double bond groups, *i.e.*, C═O and COOH, are the active sites for the hydrous hydrazine decomposition reaction.

Atomistic modeling

Systematic DFT simulations were employed to unravel the role of oxygen functionalities at the atomistic scale and rationalize the catalytic performances and kinetic trends in relation to the surface species. Fig. S1† shows the four different graphitic surfaces modelled as derived from XPS, *i.e.*, C═O, C–O–C, C–OH and COOH. All the structures were optimized from relaxed graphene layers with a single vacancy to which the desired functional group was attached.[51]

Previous works on hydrazine highlighted the *cis* configuration of N_2H_4 as the most favorable for adsorption processes.[12,27,52] Therefore, *cis*-N_2H_4 was brought close to the functional group on the surface, so that the N atoms would be able to interact properly with the dangling bonds The most favourable adsorptions (Fig. 6 and S5†) led to trends as a function of the oxygenated species: C–OH (−0.82 eV) < C═O (−1.39 eV) < COOH (−1.34 eV) < C–O–C (−1.62 eV). Fig. 6 shows that the N_2H_4 interaction with C═O, C–OH and COOH promoted the N–N dissociation, leading to two NH_2 groups saturating nearby C-dangling bonds. In addition, for all the surfaces, *anti* and *gauche* configurations were tested, favoring the interaction of the dangling bonds with the N–H moieties, but the process was found to be endothermic for all the structures.

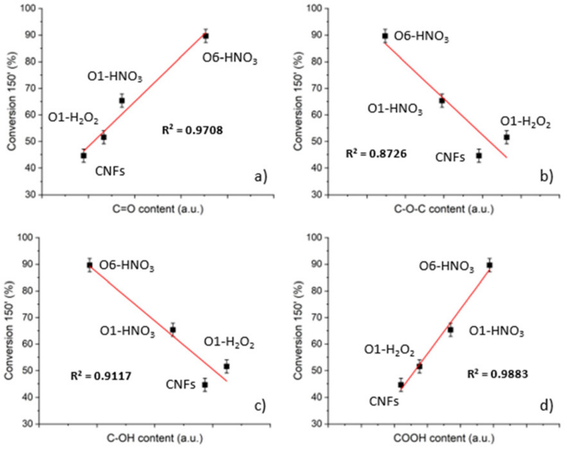

Fig. 5 Trends of conversion with respect to the total surface content of (a) C═O, (b) C–O–C, (c) C–OH and (d) COOH, as quantified from the XPS analysis. Insets are the catalyst labels and R^2 factor of the linear fit.

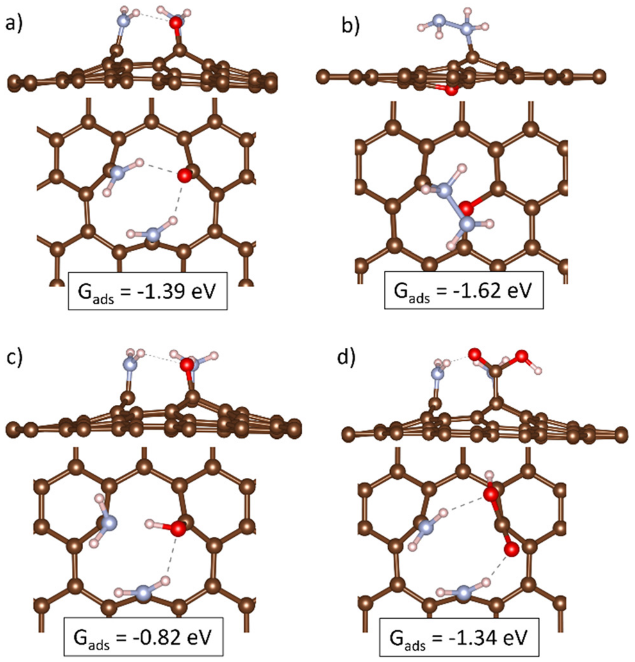

Fig. 6 Top and side views of the most favourable adsorption configurations upon interaction with N_2H_4: (a) C═O, (b) C–O–C, (c) C–OH and (d) COOH. The carbon atom is labelled brown, oxygen in red and hydrogen in white. Inset are the Gibbs adsorption energies (G_{ads}).

The initial exploration of the N_2H_4 interaction with the functionalized surface, in agreement with the previous experimental results, indicates Gibbs energies of ∼−1.3/1.4 eV to be neither too strong nor too weak to promote the N_2H_4 decomposition.[53] The strong N_2H_4 molecular adsorption on C–O–C sites may lead to surface poisoning, a hypothesis confirmed by the systematic decrease of C–O–C moieties observed in the O1s core level of the spent catalysts, Table S4.† The orientation of the adsorbates and the functional C═O and COOH groups also points to a possible H-transfer and enolate formation as part of the catalytic cycle, which C–OH cannot undertake. The exothermic adsorption on the active sites (C═O and COOH) agrees with the experimental enhanced catalytic activity observed with increasing oxygen content. In addition, we previously demonstrated that the scission of the N–N bond in the first adsorption step of hydrazine favours NH_3 formation (eqn (2))[27] and previous works on hydrazine mediated H-transfer highlighted enhanced reduction of target substrates in the presence of oxygenated carbonaceous materials.[25,26] Therefore, we explain the selectivity results of the active sites as a combined N–N dissociation and preferential H-transfer, suppressing H_2 generation as a whole.

Conclusions

A combination of computational and experimental studies was employed to elucidate the role of oxygen functionalities in carbonaceous materials for the hydrous hydrazine decomposition reaction. Three different oxygen functionalized catalysts were synthesized (O1-H_2O_2, O1-HNO_3 and O6-HNO_3) using different oxidizing agents (HNO_3 and H_2O_2) and variable times (1 and 6 h). These samples were compared to the pristine nanofibers. An enhanced catalytic activity (89%, O6-HNO_3 > 65%, O1-HNO_3 > 52%, O1-H_2O_2 > 52%, CNFs) and decreased H_2 production (8%, O6-HNO_3 < 14%, O1-HNO_3 < 35%, O1-H_2O_2 < 89%, CNFs) were observed concerning the oxidizing agents' strength and functionalization time. A thorough characterization of the catalyst through Raman spectroscopy and XPS unveiled a positive linear correlation between the oxygen content and the catalytic activity ($R^2 = 0.9459$). In contrast, a negative trend was observed for hydrogen production, although there is no linear correlation ($R^2 = 0.7129$). A targeted analysis of O1s and C1s core levels and kinetic data assigned carbon–oxygen double bond groups (COOH and C═O) as active sites. The adsorption of hydrazine on graphitic surfaces resembling those derived from XPS was simulated using DFT, resulting in a preferential N–N breakage at the active sites (C═O and COOH). These groups may form enolate intermediates, favouring the NH_3 and explaining the experimental trends in H_2 selectivity.

Author contributions

Conceptualization, A. V.; validation, A. V. and A. R.; formal analysis, investigation and writing – original draft preparation, S. B. Writing – review and editing, A. R., I. B., P. F., and S.T. All authors have read and agreed to the published version of the manuscript.

Conflicts of interest

There are no conflicts to declare.

Acknowledgements

This research is part of the project "One Health Action Hub: University Task Force for the resilience of territorial ecosystems", supported by Università degli Studi di Milano – PSR 2021 – GSA. We acknowledge the computing time at the facilities of Supercomputing Wales and the Advanced Research Computing Cardiff (ARCCA) at Cardiff University.

References

1 T. N. Veziroğlu and S. Şahin, *Energy Convers. Manage.*, 2008, **49**, 1820–1831.
2 P. Nikolaidis and A. Poullikkas, *Renewable Sustainable Energy Rev.*, 2017, **67**, 597–611.
3 H. T. Hwang and A. Varma, *Curr. Opin. Chem. Eng.*, 2014, **5**, 42–48.
4 D. Pukazhselvan, V. Kumar and S. K. Singh, *Nano Energy*, 2012, **1**, 566–589.
5 J. K. Norskov and C. H. Christensen, *Science*, 2006, **312**, 1322–1323.
6 Z. Zhang, S. Zhang, Q. Yao, X. Chen and Z.-H. Lu, *Inorg. Chem.*, 2017, **56**, 11938–11945.
7 S. J. Cho, J. Lee, Y. S. Lee and D. P. Kim, *Catal. Lett.*, 2006, **109**, 181–186.
8 A. K. Singh, M. Yadav, K. Aranishi and Q. Xu, *Int. J. Hydrogen Energy*, 2012, **37**, 18915–18919.
9 P.-X. Zhang, Y.-G. Wang, Y.-Q. Huang, T. Zhang, G.-S. Wu and J. Li, *Catal. Today*, 2011, **165**, 80–88.
10 S. Bellomi, I. Barlocco, X. Chen, J. J. Delgado, R. Arrigo, N. Dimitratos, A. Roldan and A. Villa, *Phys. Chem. Chem. Phys.*, 2023, **25**, 1081–1095.
11 D. Motta, I. Barlocco, S. Bellomi, A. Villa and N. Dimitratos, *Nanomaterials*, 2021, **11**, 1340.
12 S. S. Tafreshi, A. Roldan and N. H. de Leeuw, *Phys. Chem. Chem. Phys.*, 2015, **17**, 21533–21546.
13 W. Kang, H. Guo and A. Varma, *Appl. Catal., B*, 2019, **249**, 54–62.
14 L. Zhou, X. Luo, L. Xu, C. Wan and M. Ye, *Catalysts*, 2020, **10**, 8.
15 L. He, B. Liang, L. Li, X. Yang, Y. Huang, A. Wang, X. Wang and T. Zhang, *ACS Catal.*, 2015, **5**, 1623–1628.
16 K. S. Sanjay, X. B. Zhang and Q. Xu, *J. Am. Chem. Soc.*, 2009, **131**, 9894–9895.
17 X. Lu, S. Francis, D. Motta, N. Dimitratos and A. Roldan, *Phys. Chem. Chem. Phys.*, 2020, **22**, 3883–3896.
18 N. Gupta, O. Khavryuchenko, A. Villa and D. Su, *ChemSusChem*, 2017, **10**, 3030–3034.
19 M. S. Shafeeyan, W. M. A. W. Daud, A. Houshmand and A. Arami-Niya, *Appl. Surf. Sci.*, 2011, **257**, 3936–3942.
20 I. Barlocco, S. Capelli, X. Lu, S. Tumiati, N. Dimitratos, A. Roldan and A. Villa, *Nanoscale*, 2020, **12**, 22768–22777.
21 J. Zhang, D. S. Su, R. Blume, R. Schlögl, R. Wang, X. Yang and A. Gajović, *Angew. Chem., Int. Ed.*, 2010, **49**, 8640–8644.
22 T. Hirashima and O. Manabe, *Chem. Lett.*, 1975, **4**, 259–260.
23 G. R. Srinivasa, K. Abiraj and D. C. Gowda, *Indian J. Chem. - Sect. B Org. Med. Chem.*, 2003, **42**, 2885–2887.
24 D. Cantillo, M. M. Moghaddam and C. O. Kappe, *J. Org. Chem.*, 2013, **78**, 4530–4542.
25 J. W. Larsen, M. Freund, K. Y. Kim, M. Sidovar and J. L. Stuart, *Carbon*, 2000, **38**, 655–661.
26 S. Fujita, H. Watanabe, A. Katagiri, H. Yoshida and M. Arai, *J. Mol. Catal. A: Chem.*, 2014, **393**, 257–262.
27 I. Barlocco, S. Bellomi, S. Tumiati, P. Fumagalli, N. Dimitratos, A. Roldan and A. Villa, *Phys. Chem. Chem. Phys.*, 2022, **24**, 3017–3029.
28 C. Gojon and B. Dureault, *J. Nucl. Sci. Technol.*, 1996, **33**, 731–735.
29 R. Arrigo, M. Hävecker, S. Wrabetz, R. Blume, M. Lerch, J. McGregor, E. P. J. Parrott, J. A. Zeitler, L. F. Gladden, A. Knop-Gericke, R. Schlögl and D. S. Su, *J. Am. Chem. Soc.*, 2010, **132**, 9616–9630.

30 G. Kresse and J. Furthmüller, *Phys. Rev. B: Condens. Matter Mater. Phys.*, 1996, **54**, 11169–11186.
31 G. Kresse, *J. Non-Cryst. Solids*, 1995, **192–193**, 222–229.
32 B. Hammer, L. B. Hansen and J. K. Nørskov, *Phys. Rev. B: Condens. Matter Mater. Phys.*, 1999, **59**, 7413–7421.
33 N. D. Mermin, *Phys. Rev.*, 1965, **137**, 1–3.
34 Y. Zhang and W. Yang, *Phys. Rev. Lett.*, 1998, **80**, 890.
35 R. Sure, J. Antony and S. Grimme, *J. Phys. Chem. B*, 2014, **118**, 3431–3440.
36 S. Ehrlich, J. Moellmann, W. Reckien, T. Bredow and S. Grimme, *ChemPhysChem*, 2011, **12**, 3414–3420.
37 R. Sundararaman and K. Schwarz, *J. Chem. Phys.*, 2017, **146**(8), DOI: 10.1063/1.4976971.
38 K. Mathew, R. Sundararaman, K. Letchworth-Weaver, T. A. Arias and R. G. Hennig, *J. Chem. Phys.*, 2014, **140**(8), DOI: 10.1063/1.4865107.
39 J. D. Pack and H. J. Monkhorst, *Phys. Rev. B: Solid State*, 1977, **16**, 1748–1749.
40 Y. W. Tan, H. L. Stormer, P. Kim, K. S. Novoselov, M. L. Cohen, S. G. Louie, X. Wang, L. Zhang, S. Lee, H. Dai, Y. Kobayashi, K. Fukui, M. Fujita, G. Dresselhaus, M. S. Dresselhaus, M. A. Pimenta, B. R. A. Neves, A. Jorio, Y. Zhang, M. Mailman, P. M. Ajayan, S. K. Nayak, C. H. Park, Y. W. Son, S. P. Lu, S. Piscanec, A. C. Ferrari, G. Dobrik, P. Lambin, A. Oberlin, T. Solid, K. Suenaga, S. Iijima, P. Hermet, V. Meunier, L. Henrard, D. Gunlycke, C. T. White, S. Chen, B. I. Yakobson and S. Gradecak, *Science*, 2009, **323**, 1705–1708.
41 I. Barlocco, L. A. Cipriano, G. Di Liberto and G. Pacchioni, *J. Catal.*, 2023, **417**, 351–359.
42 M. W. Chase and N. I. S. O. (US), *NIST-JANAF thermochemical tables*, American Chemical Society Washington, DC, 1998, vol. 9.
43 L. A. Cipriano, G. Di Liberto and G. Pacchioni, *ACS Catal.*, 2022, **12**, 11682–11691.
44 S. Sengodan, R. Lan, J. Humphreys, D. Du, W. Xu, H. Wang and S. Tao, *Renewable Sustainable Energy Rev.*, 2018, **82**, 761–780.
45 S. K. Singh, A. K. Singh, K. Aranishi and Q. Xu, *J. Am. Chem. Soc.*, 2011, **133**, 19638–19641.
46 F. Tuinstra and J. L. Koenig, *J. Chem. Phys.*, 1970, **53**, 1126–1130.
47 H. Murphy, P. Papakonstantinou and T. I. T. Okpalugo, *J. Vac. Sci. Technol., B: Microelectron. Nanometer Struct.–Process., Meas., Phenom.*, 2006, **24**, 715–720.
48 V. Datsyuk, M. Kalyva, K. Papagelis, J. Parthenios, D. Tasis, A. Siokou, I. Kallitsis and C. Galiotis, *Carbon*, 2008, **46**, 833–840.
49 S.-Y. Yang, C.-C. M. Ma, C.-C. Teng, Y.-W. Huang, S.-H. Liao, Y.-L. Huang, H.-W. Tien, T.-M. Lee and K.-C. Chiou, *Carbon*, 2010, **48**, 592–603.
50 K. A. Wepasnick, B. A. Smith, K. E. Schrote, H. K. Wilson, S. R. Diegelmann and D. H. Fairbrother, *Carbon*, 2011, **49**, 24–36.
51 C. H. Lau, R. Cervini, S. R. Clarke, M. G. Markovic, J. G. Matisons, S. C. Hawkins, C. P. Huynh and G. P. Simon, *J. Nanopart. Res.*, 2008, **10**, 77–88.
52 X. Lu, S. Francis, D. Motta, N. Dimitratos and A. Roldan, *Phys. Chem. Chem. Phys.*, 2020, **22**, 3883–3896.
53 Q. Zhai, Z. Xia and L. Dai, *Catal. Today*, 2023, **418**, 114129.